Constraints on the Maximum Densities of Neutron Stars from Postmerger Gravitational Waves with Third-Generation Observations

Matteo Breschi®, ¹ Sebastiano Bernuzzi®, ¹ Daniel Godzieba®, ² Albino Perego®, ^{3,4} and David Radice® ^{5,2,6}

¹Theoretisch-Physikalisches Institut, Friedrich-Schiller-Universität Jena, 07743 Jena, Germany

²Department of Physics, Pennsylvania State University, University Park, Pennsylvania 16802, USA

³Dipartimento di Fisica, Università di Trento, Via Sommarive 14, 38123 Trento, Italy

⁴INFN-TIFPA, Trento Institute for Fundamental Physics and Applications, via Sommarive 14, I-38123 Trento, Italy

⁵Institute for Gravitation and the Cosmos, Pennsylvania State University, University Park, Pennsylvania 16802, USA

⁶Department of Astronomy and Astrophysics, Pennsylvania State University, University Park, Pennsylvania 16802, USA

(Received 22 November 2021; revised 31 January 2022; accepted 18 March 2022; published 19 April 2022)

Using data from 289 numerical relativity simulations of binary neutron star mergers, we identify, for the first time, a robust quasiuniversal relation connecting the postmerger peak gravitational-wave frequency and the value of the density at the center of the maximum mass nonrotating neutron star. This relation offers a new possibility for precision equation-of-state constraints with next-generation ground-based gravitational-wave interferometers. Mock Einstein Telescope observations of fiducial events indicate that Bayesian inferences can constrain the maximum density to $\sim 15\%$ (90% credibility level) for a single signal at the minimum sensitivity threshold for a detection. If the postmerger signal is included in a full-spectrum (inspiral-merger-postmerger) analysis of such a signal, the pressure-density function can be tightly constrained up to the maximum density, and the maximum neutron star mass can be measured with an accuracy better than 12% (90% credibility level).

DOI: 10.1103/PhysRevLett.128.161102

Introduction.—Postmerger (PM) gravitational waves (GWs) emitted from binary neutron star (BNS) merger remnants are unique probes for the stars' nuclear equation of state (EOS) at extreme densities. During merger, the neutron stars (NSs) fuse together to form a remnant NS with maximum densities up to 2 times the component's mass, reaching $\sim 3-6\rho_{\rm sat}$, where $\rho_{\rm sat} \approx 2.7 \times 10^{14} {\rm g cm}^{-3}$ is the nuclear saturation density. If the remnant does not promptly collapse to a black hole, numerical relativity (NR) simulations predict a loud GW transient emitted on dynamical timescales of tens of milliseconds with a complex signal morphology and a characteristic peak frequency $f_2 \sim 2-4$ kHz (see, e.g., [1–6]). These kilohertz GW transients have not been detected in the two BNS events GW170817 and GW190425 due to the insufficient sensitivity of the GW detectors at those frequencies [7–11]. A first detection is, however, possible (and expected) with third-generation [12,13] and other proposed detectors that specifically target the kilohertz frequencies [14]. In view of this observational scenario, it is of central importance to determine what kind of information can be extracted from PM signals and to which accuracy.

The signal-to-noise (SNR) detection threshold for a PM signal has been recently studied using different approaches (see, e.g., [15–21]). These studies found that SNRs \gtrsim 7–8 at kilohertz frequencies are typically necessary to confidently claim the detection of a BNS PM signal. These PM SNRs correspond to loud inspiral-merger signals with

SNR \ge 150 that, in turn, would provide rather accurate measurements of the binary mass and tidal polarizability parameters (see, e.g., [22–24]). While the existence of an underlining, unique EOS for the NS matter allows one to estimate the EOS at all densities from GW observations, inspiral-merger frequencies are mostly informative at the largest densities of the binary components [25–27]. In contrast, PM frequencies are expected to be mostly informative of the extreme densities reached by the remnant, although BNS PM modeling for GW inference is nontrivial. The main approach is to employ EOSinsensitive relations connecting the peak frequency f_2 , which is the most robust feature of the PM spectrum as predicted by simulations, and equilibrium properties of NSs like the radius at fiducial masses [28,29], averaged binary compactnesses [30], or the binary's tidal coupling constant κ_2^T [5]. For example, κ_2^T can be measured from f_2 to within a factor of 2 (\sim 20%) at PM SNR \sim 8 (15) [21], but the inspiral signal of the same event would deliver a measurement orders of magnitude more accurate [19], thus providing more stringent constraints on the pressure-density EOS function. A PM detection can typically provide only bounds on the maximum NS mass $M_{\text{max}}^{\text{TOV}}$ [27,31] [solution of the Tolman-Oppenheimer-Volkoff (TOV) equations], although multiple PM detections could provide a few percent measurement [32] complementary to that from an inspiral EOS inference [25,26,33]. The minimum NS radius $R_{\text{max}}^{\text{TOV}} = R(\rho_{\text{max}}^{\text{TOV}})$, i.e., the radius of a NS at maximum density $\rho_{\text{max}}^{\text{TOV}}$, is key information to constrain the NS mass-radius diagram. It can be extracted from a quasiuniversal relation with the peak PM frequency [32] and measured with an uncertainty of ~4 km at PM SNR 12 [19,34]. Stronger EOS constraints from BNS mergers will be possible by combining GW observations with other messengers (see, e.g., [35–42]).

In this Letter, we propose a new quasiuniversal relation connecting the NS maximum density to the peak PM frequency. The existence of an EOS-insensitive $\rho_{\max}^{\text{TOV}}(f_2)$ relation was suggested by previous work [31,32,43], but the relation obtained there involves the binary configurations with the largest possible mass that does not promptly collapse to black hole. Here, by introducing an effective Keplerian radius associated to f_2 , we propose a more general approach that can be applied to any binary and delivers a strong constraint already with a single detection. Employing full Bayesian PM analyses of mock signals and incorporating the expected information from the inspiralmerger signal, we demonstrate that a single GW BNS detection with the Einstein Telescope (ET) at the PM detection threshold can already deliver a ~15% measurement of $\rho_{\rm max}^{\rm TOV}$ and $M_{\rm max}^{\rm TOV}$. The novel method shows the capabilities of next-generation detectors and introduces the possibility for direct and accurate constraints on the highdensity EOS properties from observational GW data of

Effective Keplerian radius.—The PM peak frequency f_2 can be associated to an effective remnant radius using Kepler's law:

$$R_{f_2}^3 = \frac{GM}{(\pi f_2)^2},\tag{1}$$

where G is the gravitational constant and $M = m_1 + m_2$ is the total mass of the binary. While this quantity has no direct physical interpretation in terms of the remnant properties, it correlates to the maximum central density $\rho_{\rm max}^{\rm TOV}$ of a nonrotating equilibrium NS with a weak dependence on the EOS. Figure 1 shows the approximate quasiuniversal relation $\rho_{\max}^{\text{TOV}}(R_{f_2})$ for a NR sample of 289 simulations of the CoRe Collaboration [44-48]. To explore EOS variation, the simulations were performed with 14 different EOSs including piecewise polytropes [49–53], five finite-temperature nucleonic models [54–58], one finite-temperature hybrid model accounting for deconfined quark matter [48,58], and one finite-temperature hadronic model with Λ hyperons [59,60]. The majority of the sample (~85%) is simulated using microphysics, neutrino transport, and a subgrid model for magnetohydrodynamics (MHD) turbulence, that are sufficient to fully capture the features of the PM signal modeled here. For example, the highest-to-date resolution simulations of Ref. [61] suggest that the MHD effective viscosity is small and does not affect the GWs; our subgrid model is tuned to those simulations. Neutrino-induced bulk viscosity might damp radial oscillations of the remnant (which cause secondary peaks in the spectrum) and will not impact f_2 . Moreover, recent simulations with improved neutrino transport suggest that neutrino bulk viscosity is too small to have a significant impact on dynamics and GW emission [62].

The sample includes binaries with NS masses in the range 1–2 M_{\odot} and dimensionless spin magnitudes \leq 0.2. The relation $\rho_{\rm max}^{\rm TOV}(R_{f_2})$ fits to the expression

$$\rho_{\text{max}}^{\text{TOV}} = \frac{a_0 c^6}{G^3 M^2} \left[1 + a_1 \left(\frac{c^2 R_{f_2}}{GM} \right)^{1/4} \right], \tag{2}$$

where c is the speed of light and $(a_0, a_1) = (0.135905, -0.59506)$ are determined by a standard least-squared minimization method at $\chi^2 = 0.016$. The standard deviations of the calibrated coefficients a_0 and a_1 are, respectively, equal to 1.35% and 0.22%, corresponding to a relative error of 5.8% on the final prediction.

The rhs of Eq. (2) can be entirely determined from the measurement of the binary mass M and the PM peak frequency f_2 . Writing the Keplerian radius R_{f_2} in terms of f_2 , one can get a direct relation between the maximum density $\rho_{\rm max}^{\rm TOV}$ and the PM frequency, as

$$\rho_{\text{max}}^{\text{TOV}} = \frac{a_0 c^6}{G^3 M^2} \left[1 + a_1 \left(\frac{c^3}{\pi G M f_2} \right)^{1/6} \right]. \tag{3}$$

Hence, the maximum density ρ_{max}^{TOV} can be best inferred from a full-spectrum BNS GW observation. We next discuss the potential accuracy of such measurement using a mock Bayesian inference study based on match filtering techniques and a NR-informed analytical model for the PM signal.

Mock inference study.—We consider the ET design [12,63] and assume the detector is composed by three interferometers with triangular shape and power spectral density (PSD) configuration D [12]. Mock signals are simulated from two fiducial equal-mass nonspinning BNSs: a binary with mass $M=2.73~M_{\odot}$ and (a "stiff") EOS DD2 [56] and a binary with mass $M=2.6~M_{\odot}$ and (a "soft") EOS SLy [55]. Merger and PM waveforms for these BNSs from NR were already discussed in Refs. [19,64] and are employed for the PM analyses. The fiducial binaries are placed at different distances between 80 and 200 Mpc; the injected signals have PM SNRs ranging from ~6 to 14, corresponding to total SNRs from 110 to ~260. For our case study, we perform full Bayesian analyses of the PM signals at different SNRs and employ the Fisher matrix approach to estimate the uncertainties of the parameters measured from the inspiral signals.

Bayesian PM analyses are performed using the BAJES pipeline [34] and an updated version of the NRPM model for BNS PM signals [19]. NR data are injected in a segment of 1 s with a sampling rate of 16 kHz. The sampling is

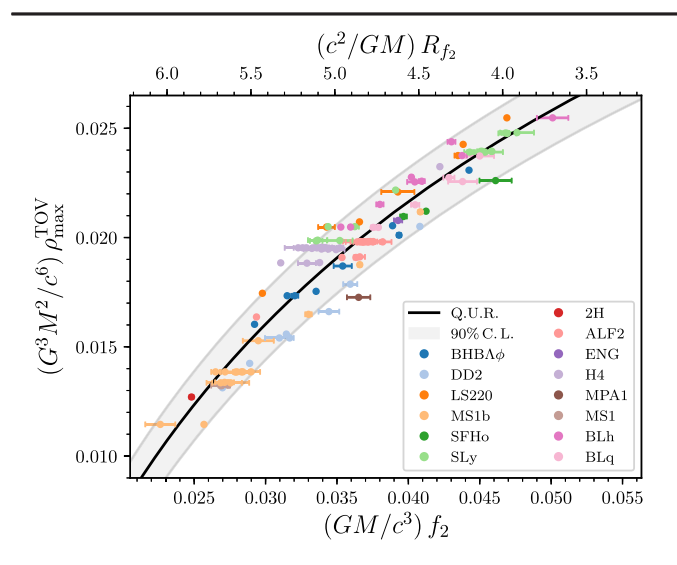


FIG. 1. Empirical relation (black line) for the maximum central density ρ_{\max}^{TOV} of a nonrotating NS as a function of the Keplerian radius R_{f_2} (top axis) and the PM peak frequency f_2 (bottom axis). The colored markers show the data extracted from 289 NR simulations with 14 EOSs. Each marker corresponds to a different binary configuration, and the error bars are computed using different numerical resolutions (when available). The shadowed area reports the 90% credibility region of the fit.

performed with DYNESTY [65] with 3200 live points analyzing the frequency region from 1 to 8 kHz. NRPM is calibrated on a subset of the numerical data shown in Fig. 1 (see [19]), and it employs a simple analytical prescription for the remnant emission to capture the three peak frequencies and damping times of typical PM signals. These (complex) frequencies, here collectively indicated as $Q^{\rm NR}$, are fully determined by the intrinsic binary properties using NR-informed quasiuniversal relations in terms of the tidal coupling constant κ_2^T and the symmetric mass ratio $\nu = m_1 m_2 / M^2$ [5,19,66]. The prior distribution is assumed to be uniform in the mass components, spanning the ranges $M \in [1.5, 6]$ M_{\odot} and $m_1/m_2 \in [1, 2]$, and in the individual NS quadrupolar tidal polarizability parameters $\Lambda_i \in$ [0,5000] for i=1, 2. Spin magnitudes are kept fixed to zero. The extrinsic parameters are treated as discussed in Ref. [34], with volumetric prior for the luminosity distance in the range [5,500] Mpc. The likelihood function is analytically marginalized over reference time and phase.

In this Letter, NRPM is extended with two sets of additional parameters that are determined by the Bayesian inference. A first set of three parameters $(\alpha, \beta, \phi_{PM})$ is introduced to enhance the flexibility of the model and to improve fitting factors to the PM signals with complex morphology. α is a damping time for the PM bursts [see Eq. (9c) of Ref. [19]]; β accounts for a linear contribution in the frequency evolution as discussed in Ref. [21]; and ϕ_{PM} is an additional phase shift corresponding to the first amplitude minimum [19]. The prior

distribution of these parameters is chosen uniformly in $\alpha^{-1} \in [1,1000], \ \beta \in [10^{-4},-10^{-4}], \ \text{and} \ \phi_{\text{PM}} \in [0,2\pi]. \ \text{A}$ second set of recalibration parameters δ_Q is introduced to account for the uncertainties of each quasiuniversal relation $Q^{\text{NR}}(\kappa_2^T,\nu)$. Specifically, we map $Q^{\text{NR}} \mapsto Q^{\text{NR}}(1+\delta_Q)$ and treat δ_Q similarly to standard calibration parameters in GW analyses (see, e.g., [67]). The prior distribution for the δ_Q is assumed to be normal with zero mean and variance prescribed by the residuals of the quasiuniversal relations.

This approach aims at combining the strengths of the NRPM templated analyses, built on quasiuniversal relations, with those of more agnostic analyses using minimal assumptions about the signal morphology (see, e.g., [16,21]). In particular, the improved NRPM model used here improves the fitting factors by an order of magnitude with respect to Ref. [19] and can detect PM GW signals at a SNR comparable to unmodeled approaches [18,21]. While relying on a larger number of parameters than unmodeled methods, NRPM can deliver a measure of the intrinsic parameters independently on premerger analyses and produces narrower f_2 posteriors for the same PM SNR. The inference of the tidal coupling constant is also improved: Comparing to Ref. [21], κ_2^T is inferred to \sim 30% for PM SNR \sim 12 instead of \sim 15. We also note that unmodeled analyses rely on analogous quasiuniversal relations to infer κ_2^T and, hence, should also consider recalibration parameters.

Fisher matrix analyses of the inspiral-merger signals are performed with GWBENCH [68]. Considering the large SNR of these signals, the Fisher matrix provides an approximation of the posterior distributions of the binary mass and tidal parameters that is sufficiently accurate for our purposes. For instance, in the lowest SNR case of 110, the uncertainty on the binary mass measured from the inspiral signal is $\sim 10^{-4}~M_{\odot}$, and the uncertainty on the quadrupolar tidal polarizability parameters is $\sim 2\%$. These results imply, as expected, that the inference on $\rho_{\rm max}^{\rm TOV}$ via Eq. (2) has uncertainties dominated by the measurement of f_2 from the PM signal and by recalibration errors.

Maximum density constraint.—Our analysis indicates that PM signals can be detected with SNRs as low as PM SNR threshold of ~7.5 (total SNR ~ 140). As shown in the top panel in Fig. 2, the SNR threshold corresponds to a Bayes' factor of log $\mathcal{B} \gtrsim 5$ in favor of the signal (vs noise) hypothesis. This detection threshold is comparable to those obtained with a minimally modeled PM waveform (see, e.g., [21]) and improves over the previous NRPM results [19] as a consequence to the enhanced flexibility of our fully NR-informed model. Figure 2 (middle panel) also shows the posterior of f_2 at different SNRs. The 90% credibility interval of the f_2 measurement is of the order of ~12% at the detectability threshold and decreases to ~3% at the largest PM SNR ~ 12. The DD2 posteriors show bimodalities for SNR ≤ 9 due to a loud first peak in the

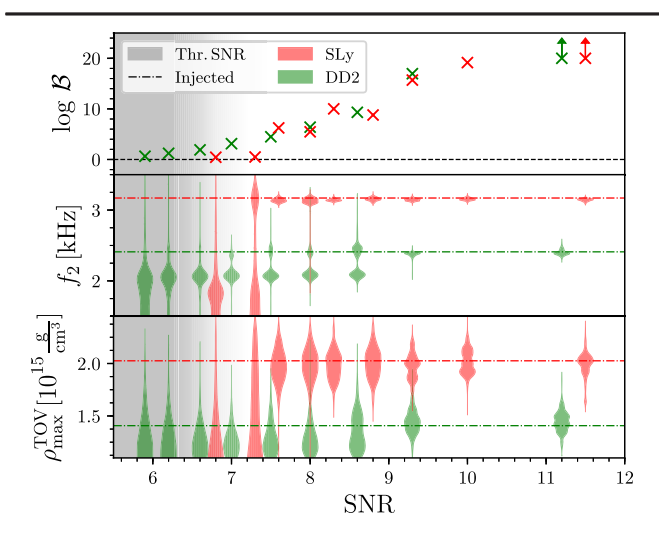


FIG. 2. Bayes' factors and posterior distributions measured in the mock inference study as functions of the PM SNR. The DD2 case is reported in green; the SLy case is reported in red. The top panel shows the recovered Bayes' factors $\log \mathcal{B}$. Central and bottom panels report the posterior distributions, respectively, of f_2 and ρ_{\max}^{TOV} , and the dash-dotted lines denote the injected values. A gray shaded region shows the detectability threshold.

spectrum (the subdominant frequency peak at frequency $f < f_2$), but this systematic vanishes for increasing SNR.

The posterior distribution for ρ_{\max}^{TOV} is obtained by combining the posteriors of M from the inspiral analysis and the posteriors of f_2 from the PM analysis. The uncertainties in the fit of Eq. (2) are taken into account with a resampling similar to the one used for the recalibration parameters (see also Ref. [42]). Analogously to the f_2 measurement, the true value is recovered at the detectability threshold with an error of ~15% at the 90% credibility level, as shown in the bottom panel in Fig. 2. Notably, the inference on ρ_{\max}^{TOV} hits the theoretical uncertainties on the quasiuniversal relation in Eq. (2) at SNR ~ 10. A more precise measure either is not possible, because at that level the relation $\rho_{\max}^{TOV}(R_{f_2})$ becomes EOS dependent, or requires a more precise quasiuniversal relation from improved simulations.

In order to further illustrate the accuracy of this approach in constraining high-density NS properties, we consider the simultaneous measure of ρ_{\max}^{TOV} and of the minimum NS radius R_{\max}^{TOV} . Here, the posteriors of (M, f_2) are mapped into $(\rho_{\max}^{TOV}, R_{\max}^{TOV})$ using Eq. (2) and the quasiuniversal relation for R_{\max}^{TOV} in Eq. (23) of Ref. [19]. As above, the uncertainties of the quasiuniversal relation are taken into account by sampling on appropriate recalibration parameters. The result is shown in Fig. 3: The injected values, denoted with crosses, confidently lay within the 90% credibility regions of the recovered posterior distributions. At the detection threshold, the uncertainty on the radius R_{\max}^{TOV} are of the order of 30% (90% credibility level). Such precision is sufficient to distinguish soft and stiff EOSs

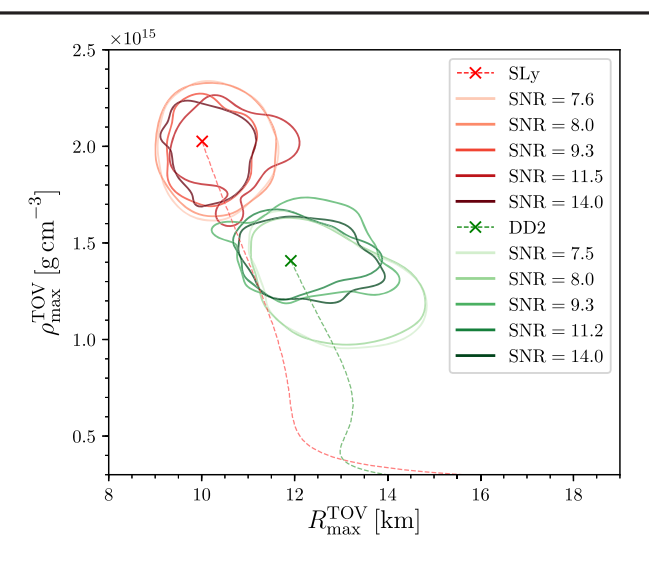


FIG. 3. Posterior distributions for $(\rho_{\max}^{TOV}, R_{\max}^{TOV})$ compared to the EOS of the injected signals. The contours show the 90% credibility regions. Green and red lines correspond, respectively, to the results obtained with DD2 and SLy EOSs, and color intensities refer to the injected SNRs of the PM data. The dashed lines show the central density as a function of the NS radius, and the crosses denote the maximum-density values.

within the 90% credibility regions, as illustrated using the SLy and DD2 EOSs.

EOS constraints and mass-radius diagram.—To illustrate the potential impact of this approach, we show how a single detection of PM signal at SNR 10 (total SNR 180 and luminosity distance of 120 Mpc) can constrain the mass-radius relation for NSs. The analysis makes use of the two-million EOS sample of Ref. [69] that is consistent with current constraints on the EOS of dense matter. In particular, all EOSs predict maximum NS mass above the maximum NS mass from pulsar observations, $M_{\text{max}}^{\text{TOV}} >$ 1.97 M_{\odot} [70], and are consistent with the upper bound on the tidal coupling constant from GW170817 [7,9,25]. The only additional assumptions are the validity of general relativity and that the EOS is causal up to the central density of the maximum mass NS. We take the SLy binary as fiducial dataset and reweight the EOS samples with the posteriors of the masses and the tidal parameters from the inspiral merger and with the maximum density and minimum radius posteriors from the PM measurement.

Figure 4 shows the 90% credibility regions of the posterior distributions in the mass-radius diagram. The inspiral-merger posteriors give the strongest constraint. They are mostly informative at the EOS at densities $\rho \simeq 2\rho_{\rm sat}$ corresponding to the individual NS components of the binary [71]. This inference leads to a measurement of the maximum NS mass of $M_{\rm max}^{\rm TOV} = 2.13_{-0.14}^{+0.20}~M_{\odot}$ (90% credibility level), consistent with the injected value (2.05 M_{\odot}). However, the EOS posterior shows a biased behavior for high mass values, i.e., $M \gtrsim 1.5~M_{\odot}$, excluding the SLy sequence from the 90% credibility region. This shows that

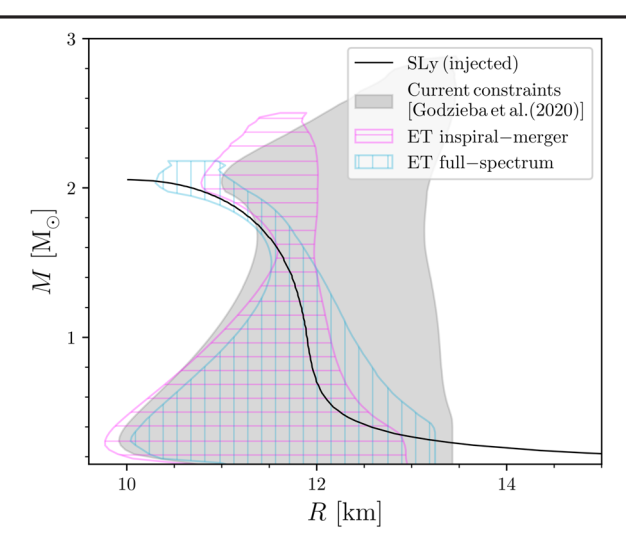


FIG. 4. Mass-radius diagram constraints from a single full-spectrum ET BNS observation with PM SNR 10 (total SNR 180). The gray area (prior) corresponds to the two-million EOS sample of Ref. [69]. The magenta and cyan areas are the 90% credibility regions given by inspiral-merger and inspiral-merger-PM inferences, respectively. The full-spectrum (cyan) posterior agrees with the injected EOS (black).

the inspiral-merger signal does not directly constrain the high-density EOS and the inferred $M_{\rm max}^{\rm TOV}$ represents an extrapolation based on the EOS representation. The inclusion of PM information strengthens the agreement with the injected EOS at higher densities allowing measurements of $M_{\rm max}^{\rm TOV} = 2.04_{-0.06}^{+0.08} \, M_{\odot}$, which agrees with the injected value and carries an error lower than 7%. The improved constraint reduces by ~60% the $p(\rho)$ posterior area of the initial EOS sample leading, in particular, to a tight pressure constraint at fiducial densities: $\log_{10}[p(2\rho_{\rm sat})/({\rm dyncm^{-2}})] = 34.52_{-0.04}^{+0.04}$ and $\log_{10}[p(4\rho_{\rm sat})/({\rm dyncm^{-2}})] = 35.39_{-0.03}^{+0.04}$ (90% credibility level). For a detection at the sensitivity threshold (PM SNR 7.5), we find that the measured maximum NS mass is $M_{\rm max}^{\rm TOV} = 2.07_{-0.09}^{+0.15} \, M_{\odot}$ with a relative error of roughly ~12%.

Outlook.—This Letter shows that next-generation GW observatories can deliver strong constraints on the extremedensity EOS from a single, full-spectrum detection of a BNS. In particular, the detection of the PM signal from the merger remnant significantly enhances the measurement of the NS maximum density and mass. The sensitivity threshold for PM BNS transients is around a luminosity distance \sim 150 Mpc, consistent with the recent estimates of Ref. [11]. According to our results, the multiple observation of about five PM BNS transients at sensitivity threshold can lead to a measurement of the maximum NS mass with an error of $\sim 5\%$ [17,21]. This information provides narrow observational constraints that would significantly inform nuclear models in the very-high-density regimes, i.e., $\rho > 3\rho_{\rm sat}$, which are unreachable conditions for modern nuclear experiments. Remarkably, the inclusion of the PM inference contributes in reducing observational errors and methodological biases.

In real observations, EOS constraints at the accuracy level reported here can be obtained by incorporating the PM signal in EOS inferences like those performed in Refs. [9,26,33,72] for inspiral-merger signals. In this context, the development of accurate EOS-insensitive relations and the determination of their validity [or their breaking (see, e.g., [73,74])] via high-precision NR simulations is a key step to improve the reliability of the GW measurement. Going beyond the Fisher matrix approach employed here, future work will consider analyses employing Bayesian methods also for the inspiral merger. Full-spectrum analyses are currently possible given the availability of complete inspiral-merger-PM waveform models [19]. The latter include correlations on the mass and tidal coupling constant between inspiral merger and PM, that will further improve the estimates of this work. However, the most urgent issue for the high-SNR inspiral mergers that will be observed by third-generation detectors remains waveform systematics in the inference of tidal properties [23,75]. Nevertheless, the computational challenges related to full-spectrum Bayesian analyses might be confronted with parallel methods [34,76] and acceleration techniques for the likelihood evaluation (see, e.g., [77–80]).

The authors thank Francesco Zappa, Aviral Prakash, and Andrea Camilletti for providing unreleased NR data and Ssohrab Borhanian for providing additional documentation for GWBENCH. Moreover, we acknowledge important discussions in the LIGO-Virgo Extreme matter group and within the Virgo-EGO Collaboration; in particular, we thank Nikolaos Stergioulas, Katerina Chatziioannou, and Jocelyn Read. M. B. and S. B. acknowledge support by the EU H2020 under ERC Starting Grant No. BinGraSp-714626. M. B. acknowledges support from the Deutsche Forschungsgemeinschaft (DFG) under Grant No. 406116891 within the Research Training Group RTG 2522/1. D. R. acknowledges funding from the U.S. Department of Energy, Office of Science, Division of Nuclear Physics under Grant No. DE-SC0021177 and from the National Science Foundation under Grants No. PHY-2011725, No. PHY-2020275, No. PHY-2116686, and No. AST-2108467. Virgo is funded by the French Centre National de Recherche Scientifique (CNRS), the Italian Istituto Nazionale della Fisica Nucleare (INFN), and the Dutch Nikhef, with contributions by Polish and Hungarian institutes. Simulations were performed on ARA, a resource of Friedrich-Schiller-Universtät Jena supported in part by DFG Grants No. INST 275/334-1 FUGG, No. INST 275/363-1 FUGG, and No. EU H2020 BinGraSp-714626. The BAJES software together with the NRPM model are publicly available [81]. The NR simulations employed in this work are publicly available [82].

- [1] M. Shibata and K. Taniguchi, Phys. Rev. D **73**, 064027 (2006).
- [2] K. Hotokezaka, K. Kiuchi, K. Kyutoku, T. Muranushi, Y.-i. Sekiguchi, M. Shibata, and K. Taniguchi, Phys. Rev. D 88, 044026 (2013).
- [3] A. Bauswein and N. Stergioulas, Phys. Rev. D 91, 124056 (2015).
- [4] K. Takami, L. Rezzolla, and L. Baiotti, Phys. Rev. Lett. 113, 091104 (2014).
- [5] S. Bernuzzi, T. Dietrich, and A. Nagar, Phys. Rev. Lett. 115, 091101 (2015).
- [6] L. Lehner, S. L. Liebling, C. Palenzuela, O. L. Caballero, E. O'Connor, M. Anderson, and D. Neilsen, Classical Quantum Gravity 33, 184002 (2016).
- [7] B. P. Abbott *et al.* (Virgo and LIGO Scientific Collaborations), Phys. Rev. Lett. **119**, 161101 (2017).
- [8] B. P. Abbott *et al.* (Virgo and LIGO Scientific Collaborations), Astrophys. J. **851**, L16 (2017).
- [9] B. P. Abbott *et al.* (LIGO Scientific and Virgo Collaborations), Phys. Rev. X **9**, 011001 (2019).
- [10] B. P. Abbott *et al.* (LIGO Scientific and Virgo Collaborations), Astrophys. J. 875, 160 (2019).
- [11] B. Abbott *et al.* (LIGO Scientific and Virgo Collaborations), Astrophys. J. Lett. **892**, L3 (2020).
- [12] S. Hild *et al.*, Classical Quantum Gravity **28**, 094013 (2011).
- [13] M. Punturo, M. Abernathy, F. Acernese, B. Allen, N. Andersson *et al.*, Classical Quantum Gravity 27, 084007 (2010).
- [14] K. Ackley et al., Pub. Astron. Soc. Aust. 37, e047 (2020).
- [15] J. A. Clark, A. Bauswein, N. Stergioulas, and D. Shoemaker, Classical Quantum Gravity 33, 085003 (2016).
- [16] K. Chatziioannou, J. A. Clark, A. Bauswein, M. Millhouse, T. B. Littenberg, and N. Cornish, Phys. Rev. D 96, 124035 (2017).
- [17] A. Torres-Rivas, K. Chatziioannou, A. Bauswein, and J. A. Clark, Phys. Rev. D 99, 044014 (2019).
- [18] K. W. Tsang, T. Dietrich, and C. Van Den Broeck, Phys. Rev. D 100, 044047 (2019).
- [19] M. Breschi, S. Bernuzzi, F. Zappa, M. Agathos, A. Perego, D. Radice, and A. Nagar, Phys. Rev. D 100, 104029 (2019).
- [20] P. J. Easter, P. D. Lasky, A. R. Casey, L. Rezzolla, and K. Takami, Phys. Rev. D 100, 043005 (2019).
- [21] P. J. Easter, S. Ghonge, P. D. Lasky, A. R. Casey, J. A. Clark, F. H. Vivanco, and K. Chatziioannou, Phys. Rev. D 102, 043011 (2020).
- [22] T. Damour, A. Nagar, and L. Villain, Phys. Rev. D 85, 123007 (2012).
- [23] R. Gamba, M. Breschi, S. Bernuzzi, M. Agathos, and A. Nagar, Phys. Rev. D 103, 124015 (2021).
- [24] K. Chatziioannou, arXiv:2108.12368.
- [25] B. P. Abbott et al. (LIGO Scientific and Virgo Collaborations), Phys. Rev. Lett. 121, 161101 (2018).
- [26] P. Landry and R. Essick, Phys. Rev. D 99, 084049 (2019).
- [27] M. Agathos, F. Zappa, S. Bernuzzi, A. Perego, M. Breschi, and D. Radice, Phys. Rev. D 101, 044006 (2020).
- [28] A. Bauswein, H. T. Janka, K. Hebeler, and A. Schwenk, Phys. Rev. D 86, 063001 (2012).
- [29] A. Bauswein, N. Stergioulas, and H.-T. Janka, Eur. Phys. J. A 52, 56 (2016).

- [30] K. Takami, L. Rezzolla, and L. Baiotti, Phys. Rev. D 91, 064001 (2015).
- [31] A. Bauswein, T. W. Baumgarte, and H. T. Janka, Phys. Rev. Lett. 111, 131101 (2013).
- [32] A. Bauswein, N. Stergioulas, and H.-T. Janka, Phys. Rev. D 90, 023002 (2014).
- [33] R. Essick, P. Landry, and D. E. Holz, Phys. Rev. D 101, 063007 (2020).
- [34] M. Breschi, R. Gamba, and S. Bernuzzi, Phys. Rev. D 104, 042001 (2021).
- [35] B. Margalit and B. D. Metzger, Astrophys. J. 850, L19 (2017).
- [36] D. Radice, A. Perego, F. Zappa, and S. Bernuzzi, Astrophys. J. 852, L29 (2018).
- [37] A. Bauswein, O. Just, H.-T. Janka, and N. Stergioulas, Astrophys. J. 850, L34 (2017).
- [38] M. W. Coughlin, T. Dietrich, Z. Doctor, D. Kasen, S. Coughlin, A. Jerkstrand, G. Leloudas, O. McBrien, B. D. Metzger, R. O'Shaughnessy, and S. J. Smartt, Mon. Not. R. Astron. Soc. 480, 3871 (2018).
- [39] G. Raaijmakers, S. K. Greif, T. E. Riley, T. Hinderer, K. Hebeler, A. Schwenk, A. L. Watts, S. Nissanke, S. Guillot, J. M. Lattimer, and R. M. Ludlam, Astrophys. J. Lett. 893, L21 (2020).
- [40] T. Dietrich, M. W. Coughlin, P. T. H. Pang, M. Bulla, J. Heinzel, L. Issa, I. Tews, and S. Antier, Science 370, 1450 (2020).
- [41] R. Essick, I. Tews, P. Landry, S. Reddy, and D. E. Holz, Phys. Rev. C 102, 055803 (2020).
- [42] M. Breschi, A. Perego, S. Bernuzzi, W. Del Pozzo, V. Nedora, D. Radice, and D. Vescovi, Mon. Not. R. Astron. Soc. 505, 1661 (2021).
- [43] G. Lioutas, A. Bauswein, and N. Stergioulas, Phys. Rev. D 104, 043011 (2021).
- [44] T. Dietrich, D. Radice, S. Bernuzzi, F. Zappa, A. Perego, B. Brügmann, S. V. Chaurasia, R. Dudi, W. Tichy, and M. Ujevic, Classical Quantum Gravity 35, 24LT01 (2018).
- [45] D. Radice, A. Perego, K. Hotokezaka, S. A. Fromm, S. Bernuzzi, and L. F. Roberts, Astrophys. J. 869, 130 (2018).
- [46] S. Bernuzzi et al., Mon. Not. R. Astron. Soc. 497, 1488 (2020).
- [47] V. Nedora, S. Bernuzzi, D. Radice, B. Daszuta, A. Endrizzi, A. Perego, A. Prakash, M. Safarzadeh, F. Schianchi, and D. Logoteta, Astrophys. J. 906, 98 (2021).
- [48] A. Prakash, D. Radice, D. Logoteta, A. Perego, V. Nedora, I. Bombaci, R. Kashyap, S. Bernuzzi, and A. Endrizzi, Phys. Rev. D 104, 083029 (2021).
- [49] L. Engvik, G. Bao, M. Hjorth-Jensen, E. Osnes, and E. Ostgaard, Astrophys. J. 469, 794 (1996).
- [50] H. Müller and B. D. Serot, Nucl. Phys. A606, 508 (1996).
- [51] M. Alford, M. Braby, M. W. Paris, and S. Reddy, Astrophys. J. 629, 969 (2005).
- [52] B. D. Lackey, M. Nayyar, and B. J. Owen, Phys. Rev. D 73, 024021 (2006).
- [53] J. S. Read, B. D. Lackey, B. J. Owen, and J. L. Friedman, Phys. Rev. D 79, 124032 (2009).
- [54] J. M. Lattimer and F. D. Swesty, Nucl. Phys. A535, 331 (1991).
- [55] F. Douchin and P. Haensel, Astron. Astrophys. 380, 151 (2001).

- [56] S. Typel, G. Ropke, T. Klahn, D. Blaschke, and H. H. Wolter, Phys. Rev. C 81, 015803 (2010).
- [57] A. W. Steiner, J. M. Lattimer, and E. F. Brown, Astrophys. J. 765, L5 (2013).
- [58] D. Logoteta, A. Perego, and I. Bombaci, Astron. Astrophys. 646, A55 (2021).
- [59] S. Banik, M. Hempel, and D. Bandyopadhyay, Astrophys. J. Suppl. Ser. 214, 22 (2014).
- [60] D. Radice, S. Bernuzzi, W. Del Pozzo, L. F. Roberts, and C. D. Ott, Astrophys. J. 842, L10 (2017).
- [61] K. Kiuchi, K. Kyutoku, Y. Sekiguchi, and M. Shibata, Phys. Rev. D 97, 124039 (2018).
- [62] D. Radice, S. Bernuzzi, A. Perego, and R. Haas, arXiv: 2111.14858.
- [63] M. Punturo, M. Abernathy, F. Acernese, B. Allen, N. Andersson *et al.*, Classical Quantum Gravity 27, 194002 (2010).
- [64] A. Perego, S. Bernuzzi, and D. Radice, Eur. Phys. J. A 55, 124 (2019).
- [65] J. S. Speagle, Mon. Not. R. Astron. Soc. 493, 3132 (2020).
- [66] F. Zappa, S. Bernuzzi, D. Radice, A. Perego, and T. Dietrich, Phys. Rev. Lett. 120, 111101 (2018).
- [67] S. Vitale, W. Del Pozzo, T. G. F. Li, C. Van Den Broeck, I. Mandel, B. Aylott, and J. Veitch, Phys. Rev. D 85, 064034 (2012).
- [68] S. Borhanian, Classical Quantum Gravity 38, 175014 (2021).

- [69] D. A. Godzieba, D. Radice, and S. Bernuzzi, Astrophys. J. 908, 122 (2021).
- [70] J. Antoniadis, P. C. Freire, N. Wex, T. M. Tauris, R. S. Lynch et al., Science 340, 6131 (2013).
- [71] M. Agathos, J. Meidam, W. Del Pozzo, T. G. F. Li, M. Tompitak, J. Veitch, S. Vitale, and C. V. D. Broeck, Phys. Rev. D 92, 023012 (2015).
- [72] B. P. Abbott *et al.* (LIGO Scientific and Virgo Collaborations), Classical Quantum Gravity **37**, 045006 (2020).
- [73] A. Bauswein, N.-U. F. Bastian, D. B. Blaschke, K. Chatziioannou, J. A. Clark, T. Fischer, and M. Oertel, Phys. Rev. Lett. 122, 061102 (2019).
- [74] C. A. Raithel and E. R. Most, arXiv:2201.03594.
- [75] A. Samajdar and T. Dietrich, Phys. Rev. D 98, 124030 (2018).
- [76] R. J. E. Smith, G. Ashton, A. Vajpeyi, and C. Talbot, Mon. Not. R. Astron. Soc. 498, 4492 (2020).
- [77] R. Smith, S. E. Field, K. Blackburn, C.-J. Haster, M. Pürrer, V. Raymond, and P. Schmidt, Phys. Rev. D 94, 044031 (2016).
- [78] B. Zackay, L. Dai, and T. Venumadhav, arXiv:1806.08792.
- [79] S. Schmidt, M. Breschi, R. Gamba, G. Pagano, P. Rettegno, G. Riemenschneider, S. Bernuzzi, A. Nagar, and W. Del Pozzo, Phys. Rev. D 103, 043020 (2021).
- [80] N. J. Cornish, Phys. Rev. D 104, 104054 (2021).
- [81] https://github.com/matteobreschi/bajes.
- [82] http://www.computational-relativity.org/.